

1 **Super-Resolution Tracking of Mitochondrial Dynamics with An Iridium(III) Luminophore**

2 Qixin Chen^{1,2,4,*}, Chengzhi Jin^{3,*}, Xintian Shao^{1,2,4,*}, Ruilin Guan^{3,*}, Zhiqi Tian¹, Chenran Wang¹, Fei

3 Liu^{2,4}, Peixue Ling^{2,4}, Jun-Lin Guan¹, Liangnian Ji³, Fengshan Wang², Hui Chao³, Jiajie Diao¹

4

5 1. Department of Cancer Biology, University of Cincinnati College of Medicine, Cincinnati, OH 45267,

6 USA.

7 2. School of Pharmaceutical Sciences, Shandong University, Jinan 250101, China.

8 3. MOE Key Laboratory of Bioinorganic and Synthetic Chemistry, School of Chemistry, Sun Yat-Sen

9 University, Guangzhou 510275, China

10 4. Shandong Academy of Pharmaceutical Science, Key Laboratory of Biopharmaceuticals, Engineering

11 Laboratory of Polysaccharide Drugs, National–Local Joint Engineering Laboratory of Polysaccharide

12 Drugs, Jinan 250101, China.

13

14 *These authors contributed equally to this work.

15 Correspondence and requests for materials should be addressed to F.W. (email: fswang@sdu.edu.cn),

16 H.C. (email: ceschh@mail.sysu.edu.cn), or J.D. (email: jiajie.diao@uc.edu).

17

18 **Abstract** Combining luminescent transition metal complex (LTMC) with super-resolution microscopy is

19 an excellent strategy for the long-term visualization of the dynamics of subcellular structures in living

20 cells. However, it remains unclear whether iridium(III) complexes are applicable for a particular type of

21 super-resolution technique, structured illumination microscopy (SIM), to image subcellular structures.

22 As described herein, we developed an iridium(III) dye, to track mitochondrial dynamics in living cells
23 under SIM. The dye demonstrated excellent specificity and photostability and satisfactory cell
24 permeability. While using SIM to image mitochondria, we achieved an approximately 80-nm resolution
25 that allowed the clear observation of the structure of mitochondrial cristae. We used the dye to monitor
26 and quantify mitochondrial dynamics relative to lysosomes, including fusion involved in mitophagy, and
27 newly discovered mitochondria-lysosome contact (MLC) under different conditions. MLC remained
28 intact and fusion vanished when five receptors, p62, NDP52, OPTN, NBR1, and TAX1BP1, were
29 knocked out, suggesting that these two processes are independence.

30

31 **Introduction**

32 Highly mobile and dynamic in living cells, mitochondria are the energy-generating organelles of cells^{1,2,}
33 ³, the disorder of which is associated with various diseases, including Alzheimer's, Parkinson's, and
34 cancer^{4,5}. Recently developed super-resolution fluorescence microscopies such as stimulated emission
35 deletion (STED)^{6, 7, 8}, structured illumination microscopy (SIM)^{9, 10, 11}, and stochastic optical
36 reconstruction microscopy (STORM)^{12,13,14}, as well as other single-molecule super-resolution imaging
37 techniques^{15, 16, 17}, are enhanced new tools for investigating the dynamics of subcellular structures,
38 including mitochondria. At the same time, they have also added to the requirements of fluorescent dyes,
39 which need especially low cytotoxicity and high photostability to make imaging living cells possible.
40 Currently, imaging subcellular structures relies upon fluorescent proteins^{18, 19}, organic dyes²⁰, and
41 quantum dots²¹; however, none of those dyes are suitable for tracking the dynamics of subcellular
42 structures due to their poor photostability and vulnerability to photobleaching²². Studies have shown that
43 using luminescent transition metal complexes (LTMCs)^{23, 24, 25, 26}, including Ru, Re, Pt, Au, and Zn, is an
44 excellent alternative strategy that can overcome those drawbacks. For example, to image mitochondria,
45 Tang et al. reported a Zn(II) complex dye whose fluorescence intensity decayed to 10% after a short
46 period of continuous scan under STORM²⁷. More recently, the lab of Jim A. Thomas developed a Ru(II)
47 complex dye with extreme photostability, large Stokes shift and subcellular targeting to image nuclear
48 chromatin and mitochondria at a resolution of less than 50 nm under STED²⁸. However, it remains
49 unclear whether third-row LTMC dyes are applicable with SIM to image the dynamics of subcellular
50 structures.

51

52 Among LTMC dyes, iridium(III) complexes are the most attractive candidate for bioimaging
53 applications due to their high phosphorescent quantum yield at room temperature, high penetration and
54 emission spectrum that can be extended to near-infrared areas, excellent photochemical and
55 physicochemical stability that allows for long-term imaging, high biological safety, and low
56 cytotoxicity^{4, 29}. Those unique structures and photophysical properties make it possible to develop
57 innovative bioimaging applications based on phosphorescence.

58
59 As described herein, we developed a small molecule dye based on iridium(III) complex for tracking
60 mitochondrial dynamics under a SIM for the first time. The dye not only has exceptional cell
61 permeability, light stability and mitochondrial specificity but can also allow the observation of
62 mitochondria at up to 80-nm resolution in living cells under SIM. Moreover, the dye permits the clear
63 observation of the structure of mitochondrial cristae, as well as the recording of dynamic approach and
64 separation processes of mitochondria. We applied the dye to monitor fusion involved in mitophagy and
65 mitochondria-lysosome contact (MLC) in living cells and found that five receptors, p62, NDP52, OPTN,
66 NBR1, and TAX1BP1, for mitophagy played no role in regulating MLC upon stimulation. Our findings
67 thus illustrate a novel perspective for using LTMC dyes such as iridium(III) complexes to image the
68 dynamic processes of subcellular structures in living cells under SIM.

69

70 **Results**

71 **Synthesis and optical characterization**

72 First, we designed and synthesized an iridium(III) complex dye with a molecular weight of 970 Da to

73 specifically image mitochondria in living cells under SIM (Fig. 1a). The main synthesis reaction route
74 consisted of three major steps (Fig. 1b), and the characterizations with electrospray mass spectrometry
75 and nuclear magnetic resonance spectroscopy appear in Supplementary Fig. 1-3. The dye had higher
76 phosphorescence at a wavelength of approximately 700 nm and different optical phosphorescence
77 characteristics in phosphate-buffered saline at pH 4-10 (Fig. 1c-d), which indicates that it can be used in
78 living cells in different pH environments. The emission spectra show that the luminescent intensity in
79 pH 4-6 is relatively low compared to that in pH 6-10. This phenomenon may contribute to the presence
80 of pyrazine ring in the auxiliary ligands of iridium(III) complexes. Since the phosphorescence intensity
81 of this iridium(III) complex is relatively stable in the pH range of 6.0 - 10.0, it is acceptable for
82 mitochondrial imaging (physiological pH: 6.50 to 8.20)³⁰. To further investigate the optical properties of
83 the dye in other solvent media, we performed fluorescence detection in 100% fetal calf serum (FBS) and
84 Dulbecco's modified eagle medium (DMEM; Supplementary Fig. 4a-b). The dye exhibited high
85 fluorescence intensity in FBS and low fluorescence in DMEM, which indicates that it can obtain a lower
86 background in DMEM under SIM. Upon testing the phosphorescence properties of the dye at different
87 temperatures, we found that it had the same optical properties at all temperatures tested (Supplementary
88 Fig. 4 c-d), which suggests using the dye can afford consistent data acquisition at physiological
89 temperature (37 °C) and ambient room temperature (25 °C) for SIM detection in living cells.

90

91 **Characterization of the iridium(III) complex dye in living cells**

92 To investigate the cell permeability of the dye in living cells, concentrations of dye ranging from 0.1 to
93 50 μ M were incubated with HeLa cells for 30 min prior to observation under a fluorescence microscope.

94 We observed high phosphorescence accumulation, and even nuclei were stained when cells were
95 exposed to dye at concentrations of 5-50 μM , whereas at concentrations of 0.1, 0.25, and 0.5 μM ,
96 phosphorescence intensity was too low to be visible (Supplementary Fig. 5). Taking both into
97 consideration, we determined that the dye at concentrations of 1 and 2.5 μM could be used to image
98 mitochondria well.

99

100 Next, we used flow cytometry to quantitatively analyze the cellular uptake of the dye (Supplementary
101 Fig. 6). Results indicated that when the cells were exposed to dye at concentrations greater than 5.0 μM ,
102 the cells took up excessive dye, whereas at a concentration less than 2.5 μM , the cellular uptake of the
103 dye gradually decreased in a dose-dependent manner. Thereafter, we evaluated the cytotoxicity of the
104 dye at concentrations of 0.1-50 μM during different durations of incubation using a CCK-8 assay
105 (Supplementary Fig. 7). Under continuous 12-hour co-culture, results revealed no significant differences
106 in cell viability between the control group and the groups treated with the dye at concentrations of less
107 than 10 μM .

108

109 Although it is feasible to observe and record dynamic progresses at the cellular level with confocal
110 optical fluorescence microscopy, it is difficult to distinguish subcellular structures at resolutions less
111 than 200 nm due to the Abbe diffraction limit^{4, 31, 32}. In response to that problem, after clarifying our
112 dye's cell permeability, high specificity, and low cytotoxicity, we investigated differences between the
113 dye imaging of mitochondria under confocal microscopy and SIM (Supplementary Fig. 8,
114 Supplementary Movies 1 & 2). To avoid the potential cytotoxicity of high-concentration dyes, we

115 selected 0.5, 1, 2.5, and 5 μM as experimental concentrations. Results revealed that the dye had a low
116 phosphorescence background in confocal microscopy and SIM, as well as that the resolution of the dye
117 at a 1 μM concentration was superior to those at 0.5, 2.5, and 0.5 μM concentrations (Supplementary Fig.
118 8c, f, i, l). When concentrations exceeded 1 μM , a large amount of the dye was taken up by the cells,
119 which caused strong phosphorescence (Supplementary Fig. 8a-f) that did not meet the requirement for
120 imaging mitochondria at the nanoscale level. By contrast, when the concentration was less than 1 μM ,
121 less dye was taken up by the cells, which resulted in weak phosphorescence due to which not even
122 mitochondrial morphology was visible (Supplementary Fig. 8i, j). Therefore, we chose 1 μM as an
123 optimal concentration for further study.

124

125 To investigate the photostability and penetration depth of the dye at 1 μM for imaging mitochondria in
126 living cells under SIM, we recorded a single mitochondrion image at every 0.2 μm of depth (Fig. 1e).
127 Results indicated that the dye had uniform tissue permeability at different depths in living cells. The
128 photobleaching properties of the dye directly affected the monitoring of mitochondrial dynamic
129 processes^{33, 34}. Next, we performed a long-term continuous laser (165 s) to stimulate cells in order to
130 monitor the photostability of the dye in the same section of the cell (Fig. 1f). We found that the dye had
131 high phosphorescence within 60 s of continuous laser stimulation and could image mitochondria within
132 135 s without photobleaching. Those properties allowed us to record more dynamic information while
133 monitoring mitochondria in living cells under SIM with the dye.

134

135 **Whole-cell 3D SIM images of mitochondrial ultrastructures using the iridium(III) complex dye**

136 Visualizing mitochondrial ultrastructures affords new understandings of the pathology and diagnosis of
137 mitochondria-related diseases^{35, 36}. To investigate the capability of obtaining more information about
138 mitochondrial ultrastructures, we used the dye to image mitochondrial ultrastructures in living cells
139 under 3D SIM. Shown in Fig. 2a, results revealed that after cell incubation with the dye for 30 min,
140 intracellular mitochondria showed spherical, rod-shaped, or filamentous particles approximately 2.0 μm
141 long (Fig. 2c-2) and approximately 0.7 μm wide (Fig. 2c-3), which is consistent with normal
142 mitochondrial volume in HeLa cells (width: 0.5-1.0 μm , length: 1.5-3.0 μm). The lamellar cristae in
143 mitochondrial were also visible using the dye—cristae thickness was approximately 105 nm (Fig. 2b,
144 Supplementary Fig. 9)—and the dye could be evenly distributed on mitochondria (Fig. 2d,
145 Supplementary Movie 3), which suggests that it can be located on the mitochondrial membrane and have
146 high specificity. To further clarify the resolution of the dye for imaging mitochondria, we obtained a
147 full-width at the half-maximum (FWHM) up to 80 nm under SIM (Fig. 2e-f), which is similar to the
148 Atto 647 mitochondrial dye reported by Han et al. (FWHM: 91 nm)³⁴. Such results suggest that our dye
149 offers higher resolution and precision for tracking mitochondria under SIM.

150

151 **Iridium(III) complex dye for tracking mitochondrial dynamics**

152 Mitochondria rank among the most dynamic organelles in cells³⁴, and understanding their dynamic
153 processes is important for analyzing the causes of many diseases³⁷. Therefore, a strategy for visualizing
154 the dynamics of mitochondria at nanoscale has important implications for understanding
155 mitochondria-related diseases. With that goal in mind, we recorded the process of mitochondrial
156 dynamics using our dye after incubating it in live cells for 30 min (Fig. 3, Supplementary Movie 4). We

157 observed that two mitochondria (Fig. 3d-f, red arrow) maintained a distance of approximately 0.6 μm in
158 Frame 1 (Fig. 3b-1) and gradually approached each other in Frames 1 and 2 (Fig. 3b, e, f). We also
159 observed the separation process of mitochondria, particularly the gradual disintegration from an intact
160 mitochondria (Fig. 3c, g-i, blue arrows), which suggests that our dye can be used to study the dynamic
161 changes such as fusion and fission of mitochondria.

162

163 **Application of the iridium(III) complex dye to track MLC and fusion**

164 The interactions of mitochondria and lysosomes, including their fusion involved in mitophagy, are
165 essential for repairing damaged mitochondria. Recently, a direct contact between mitochondria and
166 lysosome was demonstrated in normal living cells³⁸. To investigate the crosstalk of mitochondria and
167 lysosomes, we used our dye together with commercial LysoTracker Green to label lysosomes in
168 mammalian cells. We confirmed that mitochondria and lysosomes were close to each other to form MLC,
169 similar to what has been previously reported³⁸. We observed that MLC events were normal in wild-type
170 (WT) cells (Fig. 4a-f, Supplementary Movie 5-7), but did not observe fusion. Moreover, we found two
171 types of MLCs (Fig. 4c), point contact with limited overlap (Fig. 4d) and extended contact showing an
172 elongated contact surface (Fig. 4e).

173

174 For the application of our dye to image damaged mitochondria related to pathological conditions, we
175 performed another experiment with inducer treatment. We used 10.0 μM carbonyl cyanide
176 m-chlorophenyl hydrazone (CCCP), a common mitochondria damage inducer, to treat cells 12 h prior to
177 staining with our dye and LysoTracker Green. Compared to untreated cells (Fig. 4g-j, Supplementary

178 Movie 8), we observed a significant increase of large overlaps (yellow spots) of mitochondria and
179 lysosomes corresponding to the fusion after CCCP treatment.

180

181 **Iridium(III) complex dye to track MLC in Penta knockout HeLa cells**

182 MLCs were observed in both normal and stimulated conditions, while fusion involved in mitophagy was
183 only found after CCCP treatment. Pathologically, PINK1 is recruited to the mitochondrial membrane to
184 phosphorylate Ser65 of ubiquitin ligase and trigger mitophagy. During that process, several receptors
185 (i.e., p62, NDP52, OPTN, NBR1, and TAX1BP1) play an important role³⁹. Therefore, it is reasonable to
186 check whether these mitophagy proteins are involved in MLC events other than the recently reported
187 RAB7GTP hydrolysis³⁸. To investigate the correlation between MLC and fusion, we performed the SIM
188 experiment in Penta knockout (KO) HeLa cells which are deficient of mitophagy. After using 10 μ M
189 CCCP to treat cells and staining with our dye and LysoTracker Green, we found MLC events including
190 2-3 faint yellow spots for point MLC throughout the cells (Fig. 5a-c, Supplementary Movie 9). In
191 addition, we recorded the evolution of an MLC event (Fig. 5d-e, Supplementary Movie 10), in which a
192 mitochondrion and a lysosome underwent approach, contact, and separation. Meanwhile, fusion event
193 involved in mitophagy in Penta KO HeLa cells (Fig. 5a) was disappeared compared to what was found
194 in the WT HeLa cells (Fig. 4g). To that end, we performed a controlled experiment in which Penta KO
195 HeLa cells did not receive CCCP treatment. We detected no significant change of MLC events in Penta
196 KO cells (Fig. 5g, Supplementary Movie 11), which indicates that fusion between mitochondria and
197 lysosomes are independent to MLC. Again, our dye can be used to monitor MLC events in living cells.

198

199 **Quantitative analysis of the interaction between mitochondria and lysosomes**

200 To quantitatively assess the distance changes between mitochondria and lysosome under different
201 conditions, we propose a D_i -value driven from FWHM by the calculation formula shown in Fig. 6a.
202 FWHM refers to the full width of the image at half-maximum value and is a direct indicator of the
203 resolution. We then apply the D_i -value to quantify the distance change between mitochondria and
204 lysosomes under different conditions. We first calculated the D_i value (0.884 ± 0.116 , $n = 10$) in
205 untreated WT cells for MLC events. We then analyzed the D_i value of WT cells treated with CCCP. We
206 found a much lower D_i value (0.146 ± 0.118 , $n = 10$) for fusion events, indicating a significant
207 difference upon stimulation (Fig. 6b). For Penta KO cells with or without CCCP, no significant
208 difference in D_i values was observed (1.123 ± 0.176 vs 1.128 ± 0.140 , $n = 10$) (Fig. 6c).

209

210 **Discussion**

211 We discovered that a third-row transition metal complex fluorescent dye based on iridium(III) can be
212 used to track mitochondrial dynamics under SIM. Using our dye, we obtained a mitochondrial image
213 with approximately 80-nm resolution. We observed mitochondrial cristae and recorded the dynamic
214 approach and separation of mitochondria. Our results provide a novel perspective on using LTMC dyes
215 such as an iridium(III) complex to image the dynamic process of subcellular structures in living cells
216 under SIM. Given the synthesis of the iridium(III) complex, future work could focus on developing a
217 variety of novel iridium(III) dyes for the specific imaging of lysosomes, mitochondria, cell membranes,
218 nuclei, and other organelles under SIM toward the eventual goal of mapping the organelle interaction
219 network and thereby clarifying the network's establishment, maintenance, dynamic changes, and

220 regulatory mechanisms and to reveal its physiological and pathological functions.

221

222 Mitochondrial dynamic processes including fusion and fission are closely related to many diseases⁴⁰.

223 With our iridium(III) complex dye, we have demonstrated the capability of imaging these dynamics with

224 a high special resolution. Moreover, this new iridium(III) complex dye can also be used to quantitatively

225 study the functional crosstalk between mitochondria and lysosomes, such as the fusion and MLC. The

226 fusion between mitochondria and lysosomes is an important step of mitophagy for recycling damaged

227 mitochondria⁴¹. We observed that the fusion of mitochondria and lysosomes can be significantly

228 enhanced upon mitochondrial damage. However, the recently reported formation of MLCs differed from

229 these fusion events of mitophagy in which mitochondria targeted to lysosomes for destruction³⁸. Five

230 receptors (i.e., p62, NDP52, OPTN, NBR1, and TAX1BP1) that play essential roles in mitophagy were

231 not involved in the formation of MLCs³⁸, which suggests MLCs and mitophagy are independent

232 processes.

233

234 **Methods**

235 **Materials**

236 $\text{IrCl}_3 \cdot x\text{H}_2\text{O}$ were purchased from Alfa Aesar, 4,4'-dimethyl-2,2'-bipyridine, diatomite, selenium dioxide

237 1-phenyl-1,2-propane-dione, 2-aminobenzenethiol and benzene-1,2-diamine were purchased from J&K

238 Scientific. Lyso Tracker Green were purchased from Invitrogen (Invitrogen, Eugene, OR,USA); cell

239 counting kit-8 (CCK-8) was obtained Dojindo Laboratories (Dojindo Laboratories, Kumamoto, Japan);

240 fetal bovine serum (FBS), Dulbecco's modified Eagle's medium (DMEM), and other cell culture

241 reagents were obtained from Gibco BRL (Grand Island, NY, USA).

242

243 **Synthesis and characterization of iridium(III) complex dye**

244 The dye was synthesized by using a previously reported protocol².
245 4'-methyl-[2,2'-bipyridine]-4-carbaldehyde⁴² and the auxiliary ligand 2-methyl-3-phenylquinoxaline
246 (mpq)⁴³ were synthesized according to literature methods. The iridium(III) dimer [Ir(mpq)₂Cl]₂ was
247 synthesized by using the similar method of [Ir(ppy)₂Cl]₂⁴⁴. The synthetic process of the main ligand and
248 the iridium(III) complex were according to our previous work.

249

250 The main ligand (2-(4'-methyl-[2,2'-bipyridin]-4-yl)benzo[d]thiazole (mbbt)) was synthesized by
251 slowly dropping 2-aminobenzenethiol (196 mg, 1.55 mmol) into the EtOH solution of
252 4'-methyl-[2,2'-bipyridine]-4-carbaldehyde (297 mg, 1.5 mmol). After stirring overnight in RT, the
253 product was condensed and then recrystallized by using CH₂Cl₂/ethanol to get yellow flaky solid
254 Yield, 80.5%, 367 mg. Anal. Calcd. for C₁₈H₁₃N₃S (%): C, 71.26; H, 4.32; N, 13.85. Found (%):
255 C, 71.03; H, 4.63; N, 13.61. ¹H NMR (500 MHz, CDCl₃) δ 9.27 (s, 1H), 8.60 (d, *J* = 1.0 Hz, 2H),
256 8.42 (s, 1H), 8.11 (s, 1H), 8.00 (d, *J* = 4.5 Hz, 2H), 7.49 – 7.45 (m, 2H), 7.20 (s, 1H), 2.54 (s,
257 3H). ES-MS, (CH₃OH): *m/z* = 304.15 [M+H]⁺.

258

259 The goal iridium complex were synthesized by mixing mbbt (30.4 mg, 0.1 mmol) and [Ir(mpq)₂Cl]₂
260 (66.3 mg, 0.0525 mmol) in a degassing mixture of chloroform and MeOH (1:1, 40 ml). Then the
261 solution was refluxed overnight in argon atmosphere. After the reaction was stopped, the solvent was

262 removed and further purification was conducted by using alumina column chromatography to get
263 crimson microcrystal. Yield, 51.3%, 49.7 mg. Anal. Calcd. for $C_{48}H_{35}N_7SClIr$ (%): C, 59.46; H,
264 3.64; N, 10.11. Found (%): C, 59.19; H, 3.91; N, 10.01. 1H NMR (500 MHz, CD_3OD): δ 8.78 (d,
265 $J = 1.5$ Hz, 1H), 8.57 – 8.48 (m, 3H), 8.30 (s, 3H), 8.27 (dd, $J = 6.0, 1.5$ Hz, 1H), 8.23 (d, $J = 6.0$
266 Hz, 1H), 8.08 (t, $J = 8.0$ Hz, 2H), 7.87 (t, $J = 8.0$ Hz, 2H), 7.59 (s, 1H), 7.57 – 7.51 (m, 4H), 7.42
267 (t, $J = 10.0$ Hz, 2H), 7.32 – 7.26 (m, 2H), 7.11 (d, $J = 12.0$ Hz, 2H), 6.89 (d, $J = 8.0$ Hz, 2H),
268 6.72 (dd, $J = 18.0, 7.5$ Hz, 2H), 3.40 (d, $J = 15.1$ Hz, 6H), 2.49 (s, 3H). ^{13}C NMR (125 MHz,
269 CD_3OD) δ 164.62, 164.55, 162.30, 156.57, 154.36, 153.18, 152.99, 152.87, 152.81, 152.68,
270 148.37, 146.82, 144.41, 143.47, 140.06, 139.90, 139.85, 130.62, 130.59, 129.97, 129.88, 129.80,
271 129.17, 128.66, 127.15, 127.01, 125.14, 125.01, 123.74, 122.98, 122.02, 120.63, 26.14, 26.09,
272 19.79. ES-MS (CH_3OH): $m/z = 933.95 [M-Cl]^+$.

273

274 1H and ^{13}C NMR spectra were recorded using a Bruker 500 Nuclear Magnetic Resonance
275 Spectrometer using $CDCl_3$ or CD_3OD as the deuterated solvent. The electronic absorption
276 spectra were recorded using a Perkin-Elmer Lambda 850 UV/Vis spectrometer. The emission
277 spectra were recorded using a Perkin-Elmer LS 55 luminescence spectrometer and FLS 980
278 luminescence spectrometer. Microanalysis (C, H, and N) was carried out using an Elemental
279 Vario EL elemental analyzer. Electro spray mass spectra were recorded using an LCQ system
280 (Finnigan MAT, USA).

281

282 **Cell culture**

283 HeLa cells were gifted from Dr. Carolyn M. Price lab (University of Cincinnati). Penta knockout HeLa
284 cells were gifted from Dr. Richard J. Youle lab (National Institutes of Health). Cells were cultured in
285 Dulbecco's modified Eagle medium supplemented with 10% FBS, penicillin (100 units/ml), and
286 streptomycin (100 µg/ml) in a 5% CO₂ humidified incubator at 37 °C.

287

288 **Cell viability and cytotoxicity assay**

289 Cells were treated in a 96-well plate at density of 5×10^5 cell/ml. The viability was determined by using
290 a cell counting kit-8 (CCK-8). 10 µl CCK-8 solution was added to each well and the OD value for each
291 well was read at wavelength 450 nm on a microplate reader (Multiskan, Thermo, USA).

292

293 **Flow cytometry analysis**

294 Cells were seeded on 6-well plate at density of 1×10^5 cell/ml in 1 ml of complete medium for 24 h.
295 After treatment with iridium(III) complex dye (0.1, 0.25, 0.5, 1, 2.5, 5, 10, 25, and 50 µM) for 30 min,
296 cells were collected by trypsinization and washed 2 times with cool PBS. Cells were resuspended by 500
297 µl binding buffer while avoiding light prior to detection by flow cytometry.

298

299 **Live cell labeling**

300 Cells were incubated with 1 µM IR for 30 min in free DMEM, and washed with free DMEM 3 times and
301 observed using a fluorescence microscope (CX41-32RFL; Olympus, Japan), confocal laser scanning
302 microscopy or OMX 3D-SIM super-resolution microscope.

303

304 **Confocal laser scanning microscopy**

305 The images were obtained using a LSM-710 confocal laser scanning microscope (Carl Zeiss, Inc.)
306 equipped with a $63\times/1.49$ numerical aperture oil-immersion objective lens and were analyzed with ZEN
307 2012 (Carl Zeiss, Inc.) and ImageJ software (National Institutes of Health). All fluorescence images
308 were analyzed and the background subtracted with ImageJ software. Pearson's coefficient was
309 quantified using the Colocalization Analysis plugin for ImageJ.

310

311 **OMX 3D-SIM super-resolution microscope imaging**

312 Super-resolution images were acquired on OMX 3D-SIM Microscope (Bioptechs, Inc) equipped with a
313 Olympus $100\times/1.49$ numerical aperture oil-immersion objective lens and solid-state lasers. Images were
314 captured with an electron-multiplying charge coupled device (EMCCD) camera (Photometrics Cascade
315 II) with a gain value of 3000 at 10 MHz. The exposure time was set to 50 ms for each raw data capture.
316 Picture was obtained at 512×512 using Z-stacks with step size of $0.2 \mu\text{m}$. SIM frames were deliberately
317 spaced at 1-s, 2-s, 8-s or 15-s intervals according to the purpose of each experiment. SIM images were
318 analyzed with Nikon Elements and ImageJ software.

319

320 **Competing financial interests**

321 The authors declare no competing financial interests.

322

323 **Acknowledgments**

324 This research was supported by 973 Program (Nos. 2015CB856301 and 2015CB856304) from Ministry

325 of Science and Technology of China, the National Science Foundation of China (Nos. 21525105,
326 21471164, 21778079 and 21701196), the Fundamental Research Funds for the Central Universities
327 (71gjc11), China Postdoctoral Science Foundation (20173100041090767), Natural Science Foundation
328 of Shandong Province (ZR2017PH072), Key Research and Development Plan of Shandong
329 Province(2018GSF121033), and National Institutes of Health (NIH, R01NS094144 and R01CA211066
330 to J.G.). The Light Microscopy Imaging Center (LMIC) is supported in part with funds from Indiana
331 University Office of the Vice Provost for Research. The OMX 3D-SIM microscope was provided by
332 NIH grant S10 RR028697. We also thank Dr. Ehmer Birgit at University of Cincinnati for assistance
333 with laser scanning confocal microscope and flow cytometry.

334

335 **Author contributions**

336 C.J., R.G. and H.C. designed, synthesized and characterized iridium(III) complex dye. Q.C. and Z.T.
337 collected all OMX 3D-SIM super-resolution microscope data. Q.C and X.S. analyzed and processed the
338 OMX 3D-SIM data. Q.C., X.S., and C.W. cultured cell and performed confocal laser scanning
339 microscopy. F.L. performed cytotoxicity assay and flow cytometry analysis. J.G., L.J., F.W., H.C., and
340 J.D. conceived the project, designed the experiments, and wrote the manuscript with the help of all
341 authors.

342

343 **References**

- 344 1. Arasaki K, Mikami Y, Shames SR, Inoue H, Wakana Y, Tagaya M. Legionella effector Lpg1137
345 shuts down ER-mitochondria communication through cleavage of syntaxin 17. *Nature*
346 *Communications* **8**, (2017).

347

348 2. Jin CZ, *et al.* Rational design of NIR-emitting iridium(III) complexes for multimodal
349 phosphorescence imaging of mitochondria under two-photon excitation. *Chemical*
350 *Communications* **53**, 10374-10377 (2017).

351

352 3. Picard M, *et al.* Trans-mitochondrial coordination of cristae at regulated membrane junctions.
353 *Nature Communications* **6**, (2015).

354

355 4. Huang H, *et al.* Real-time tracking mitochondrial dynamic remodeling with two-photon
356 phosphorescent iridium (III) complexes. *Biomaterials* **83**, 321-331 (2016).

357

358 5. Sun L, *et al.* Iridium (III) anthraquinone complexes as two - photon phosphorescence probes for
359 mitochondria imaging and tracking under hypoxia. *Chemistry-A European Journal* **22**,
360 8955-8965 (2016).

361

362 6. Watanabe S, *et al.* Protein localization in electron micrographs using fluorescence nanoscopy.
363 *Nature Methods* **8**, 80-U117 (2011).

364

365 7. Heller I, *et al.* STED nanoscopy combined with optical tweezers reveals protein dynamics on
366 densely covered DNA. *Nature Methods* **10**, 910-U132 (2013).

367

368 8. Li DY, Qin W, Xu B, Qian J, Tang BZ. AIE Nanoparticles with High Stimulated Emission
369 Depletion Efficiency and Photobleaching Resistance for Long-Term Super-Resolution. *Adv*
370 *Mater* **29**, (2017).

371

372 9. Li D, *et al.* Extended-resolution structured illumination imaging of endocytic and cytoskeletal
373 dynamics. *Science* **349**, (2015).

374

375 10. Huang X, *et al.* Fast, long-term, super-resolution imaging with Hessian structured illumination
376 microscopy. *Nat Biotechnol*, (2018).

377

378 11. Shao L, Kner P, Rego EH, Gustafsson MGL. Super-resolution 3D microscopy of live whole cells
379 using structured illumination. *Nature Methods* **8**, 1044-+ (2011).

380

381 12. Wombacher R, *et al.* Live-cell super-resolution imaging with trimethoprim conjugates. *Nature*
382 *Methods* **7**, 717-719 (2010).

383

384 13. Huang B, Jones SA, Brandenburg B, Zhuang XW. Whole-cell 3D STORM reveals interactions
385 between cellular structures with nanometer-scale resolution. *Nature Methods* **5**, 1047-1052
386 (2008).

387

- 388 14. Jones SA, Shim SH, He J, Zhuang XW. Fast, three-dimensional super-resolution imaging of live
389 cells. *Nature Methods* **8**, 499-U496 (2011).
390
- 391 15. Ha T, Tinnefeld P. Photophysics of Fluorescent Probes for Single-Molecule Biophysics and
392 Super-Resolution Imaging. *Annu Rev Phys Chem* **63**, 595-617 (2012).
393
- 394 16. Huang B, Bates M, Zhuang XW. Super-Resolution Fluorescence Microscopy. *Annu Rev Biochem*
395 **78**, 993-1016 (2009).
396
- 397 17. Subach FV, Patterson GH, Manley S, Gillette JM, Lippincott-Schwartz J, Verkhusha VV.
398 Photoactivatable mCherry for high-resolution two-color fluorescence microscopy. *Nature*
399 *Methods* **6**, 153-159 (2009).
400
- 401 18. Day RN, Davidson MW. The fluorescent protein palette: tools for cellular imaging. *Chemical*
402 *Society Reviews* **38**, 2887-2921 (2009).
403
- 404 19. Grimm JB, *et al.* A general method to improve fluorophores for live-cell and single-molecule
405 microscopy. *Nature methods* **12**, 244 (2015).
406
- 407 20. Kim HM, Cho BR. Small-molecule two-photon probes for bioimaging applications. *Chemical*
408 *reviews* **115**, 5014-5055 (2015).
409
- 410 21. Wolfbeis OS. An overview of nanoparticles commonly used in fluorescent bioimaging. *Chemical*
411 *Society Reviews* **44**, 4743-4768 (2015).
412
- 413 22. Chen Y, Rees TW, Ji L, Chao H. Mitochondrial dynamics tracking with iridium (III) complexes.
414 *Current opinion in chemical biology* **43**, 51-57 (2018).
415
- 416 23. Saeed HK, *et al.* Homo- and Heteroleptic Phototoxic Dinuclear Metallo-Intercalators Based on
417 Ru-II(dppn) Intercalating Moieties: Synthesis, Optical, and Biological Studies. *Angew Chem Int*
418 *Edit* **56**, 12628-12633 (2017).
419
- 420 24. Fernandez-Moreira V, Thorp-Greenwood FL, Coogan MP. Application of d(6) transition metal
421 complexes in fluorescence cell imaging. *Chemical Communications* **46**, 186-202 (2010).
422
- 423 25. Nam SH, *et al.* Long-Term Real-Time Tracking of Lanthanide Ion Doped Upconverting
424 Nanoparticles in Living Cells. *Angew Chem Int Edit* **50**, 6093-6097 (2011).
425
- 426 26. Zhang PY, *et al.* A NIR phosphorescent osmium(II) complex as a lysosome tracking reagent and
427 photodynamic therapeutic agent. *Chemical Communications* **53**, 12341-12344 (2017).
428

- 429 27. Tang J, *et al.* A photoactivatable Znsalen complex for super-resolution imaging of mitochondria
430 in living cells. *Chemical Communications* **52**, 11583-11586 (2016).
431
- 432 28. Sreedharan S, *et al.* Multimodal Super-resolution Optical Microscopy Using a
433 Transition-Metal-Based Probe Provides Unprecedented Capabilities for Imaging Both Nuclear
434 Chromatin and Mitochondria. *Journal of the American Chemical Society* **139**, 15907-15913
435 (2017).
436
- 437 29. You Y. Phosphorescence bioimaging using cyclometalated Ir (III) complexes. *Current opinion in*
438 *chemical biology* **17**, 699-707 (2013).
439
- 440 30. Chen Y, Zhu C, Cen J, Bai Y, He W, Guo Z. Ratiometric detection of pH fluctuation in
441 mitochondria with a new fluorescein/cyanine hybrid sensor. *Chemical science* **6**, 3187-3194
442 (2015).
443
- 444 31. Schermelleh L, *et al.* Subdiffraction multicolor imaging of the nuclear periphery with 3D
445 structured illumination microscopy. *Science* **320**, 1332-1336 (2008).
446
- 447 32. Huang B, Babcock H, Zhuang XW. Breaking the Diffraction Barrier: Super-Resolution Imaging
448 of Cells. *Cell* **143**, 1047-1058 (2010).
449
- 450 33. Li X, Jiang M, Lam JW, Tang BZ, Qu JY. Mitochondrial Imaging with Combined Fluorescence
451 and Stimulated Raman Scattering Microscopy Using a Probe of the Aggregation-Induced
452 Emission Characteristic. *Journal of the American Chemical Society* **139**, 17022-17030 (2017).
453
- 454 34. Han Y, Li M, Qiu F, Zhang M, Zhang Y-H. Cell-permeable organic fluorescent probes for
455 live-cell long-term super-resolution imaging reveal lysosome-mitochondrion interactions. *Nature*
456 *communications* **8**, 1307 (2017).
457
- 458 35. Kopek BG, Shtengel G, Xu CS, Clayton DA, Hess HF. Correlative 3D superresolution
459 fluorescence and electron microscopy reveal the relationship of mitochondrial nucleoids to
460 membranes. *Proceedings of the National Academy of Sciences* **109**, 6136-6141 (2012).
461
- 462 36. Manji H, *et al.* Impaired mitochondrial function in psychiatric disorders. *Nature Reviews*
463 *Neuroscience* **13**, 293 (2012).
464
- 465 37. Buck MD, *et al.* Mitochondrial dynamics controls T cell fate through metabolic programming.
466 *Cell* **166**, 63-76 (2016).
467
- 468 38. Wong YC, Ysselstein D, Krainc D. Mitochondria-lysosome contacts regulate mitochondrial
469 fission via RAB7 GTP hydrolysis. *Nature* **554**, 382 (2018).

470

471 39. Lazarou M, *et al.* The ubiquitin kinase PINK1 recruits autophagy receptors to induce mitophagy.
472 *Nature* **524**, 309 (2015).

473

474 40. Chan DC. Mitochondrial fusion and fission in mammals. *Annu Rev Cell Dev Biol* **22**, 79-99
475 (2006).

476

477 41. Youle RJ, Narendra DP. Mechanisms of mitophagy. *Nature reviews Molecular cell biology* **12**, 9
478 (2011).

479

480 42. Peek BM, Ross GT, Edwards SW, Meyer GJ, Meyer TJ, Erickson BW. Synthesis of redox
481 derivatives of lysine and related peptides containing phenothiazine or tris (2, 2' - bipyridine)
482 ruthenium (II). *Chemical Biology & Drug Design* **38**, 114-123 (1991).

483

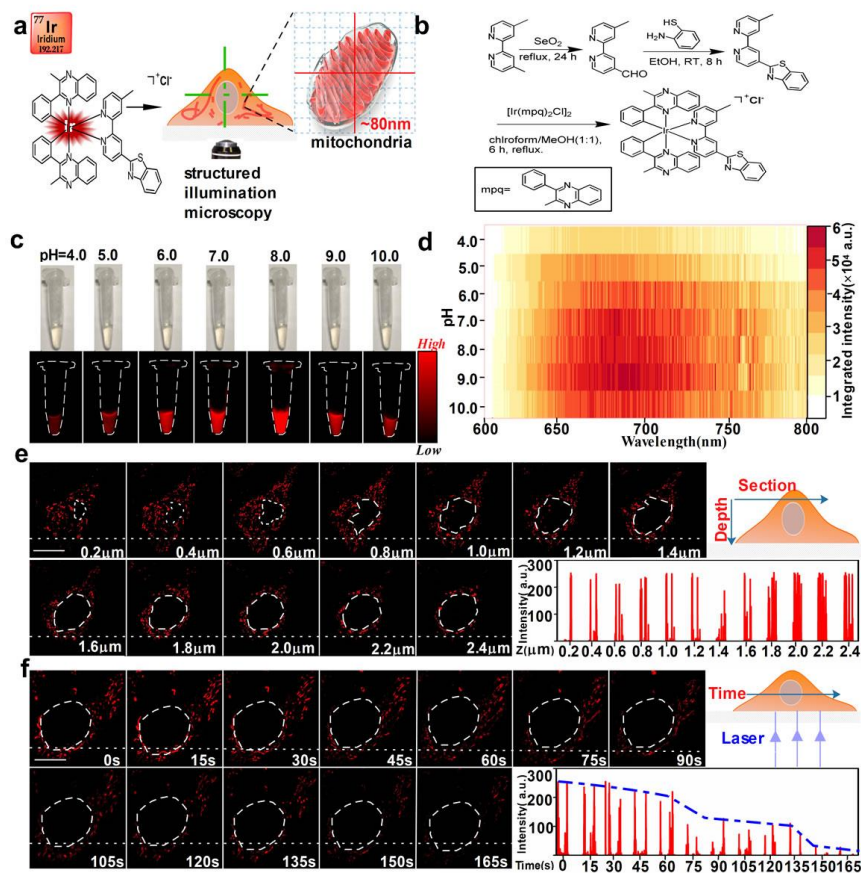
484 43. Zhang Z, Du H. A Highly cis - Selective and Enantioselective Metal - Free Hydrogenation of 2,
485 3 - Disubstituted Quinoxalines. *Angewandte Chemie International Edition* **54**, 623-626 (2015).

486

487 44. Nonoyama M. Benzo [h] quinolin-10-yl-N Iridium (III) Complexes. *Bulletin of the Chemical*
488 *Society of Japan* **47**, 767-768 (1974).

489

490



491

492 **Figure 1 Synthesis and optical characterization of the iridium(III) complex dye.** (a) Schematic

493 representation of the iridium(III) complex dye while imaging mitochondria under SIM. (b) Synthesis

494 route of the iridium(III) complex dye. (c) Fluorescence image of the iridium(III) complex dye in

495 phosphate-buffered saline at different pH levels. (d) Photoluminescence mapping of the iridium(III)

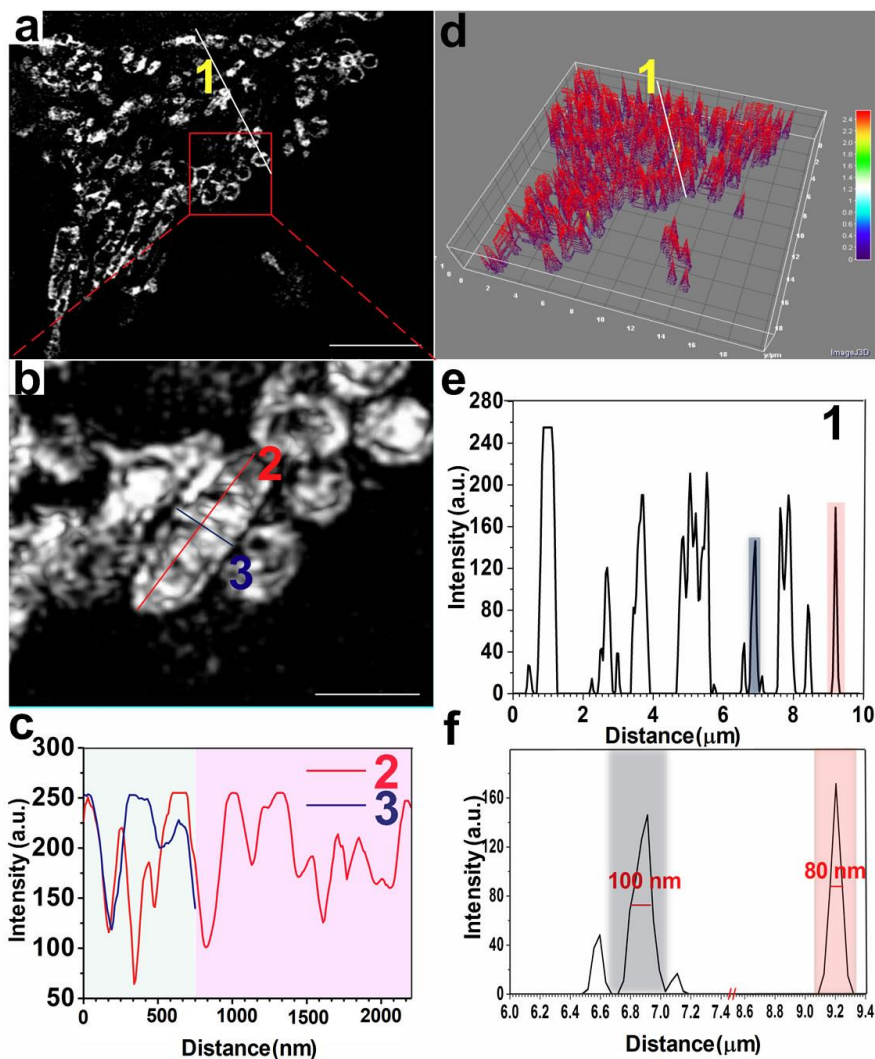
496 complex dye. (e) Mitochondrial images at different depths using the iridium(III) complex dye. White

497 dotted lines show fluorescence intensity of a single mitochondrion image at every depth of 0.2 μm. (f)

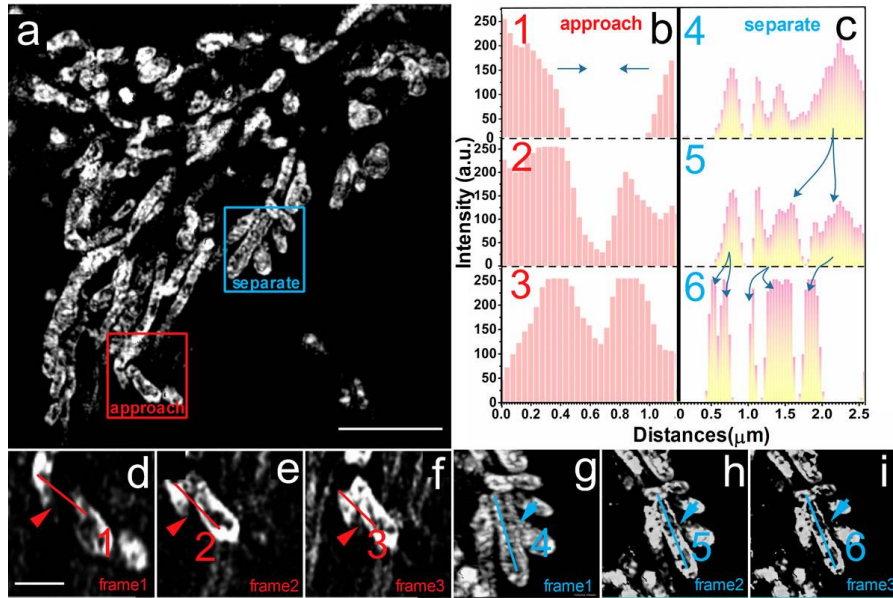
498 Photobleaching properties of the iridium(III) complex dye under laser stimulation for 165 s continuously

499 recorded in living cells. SIM frames were deliberately spaced at 15-s intervals. Scale bars: (e) 5 μm, (f) 5

500 μm.



501
502 **Figure 2 Iridium(III) complex dye images of mitochondrial ultrastructure.** (a) Iridium(III) complex
503 dye images of mitochondria in 1 μM concentration under 3D SIM. White solid line 1 shows
504 fluorescence intensity, and red rectangle shows partial amplification. (b) Single mitochondrial local
505 enlargement of (a). Red solid line 2 shows the length of a single mitochondrion, and blue solid line 3
506 shows its width. (c) Individual mitochondria fluorescence intensity with length as red solid line 2 and
507 width as blue solid line 3. (d) iridium(III) complex dye 3D map distributed in mitochondria under SIM.
508 (e) Fluorescent intensity distribution of white solid line 1. (f) Local magnification of (e), with resolution
509 of iridium(III) complex dye image of mitochondria up to 80 nm. Scale bars: (a) 5 μm , (b) 1 μm .



510

511 **Figure 3 Iridium(III) complex dye tracking of mitochondrial dynamics under SIM. (a)** Iridium(III)

512 complex dye images of mitochondria under SIM. Red rectangles indicate dynamic processes of

513 approach, and blue rectangles indicate dynamic processes of separation. **(b)** Trend of fluorescence

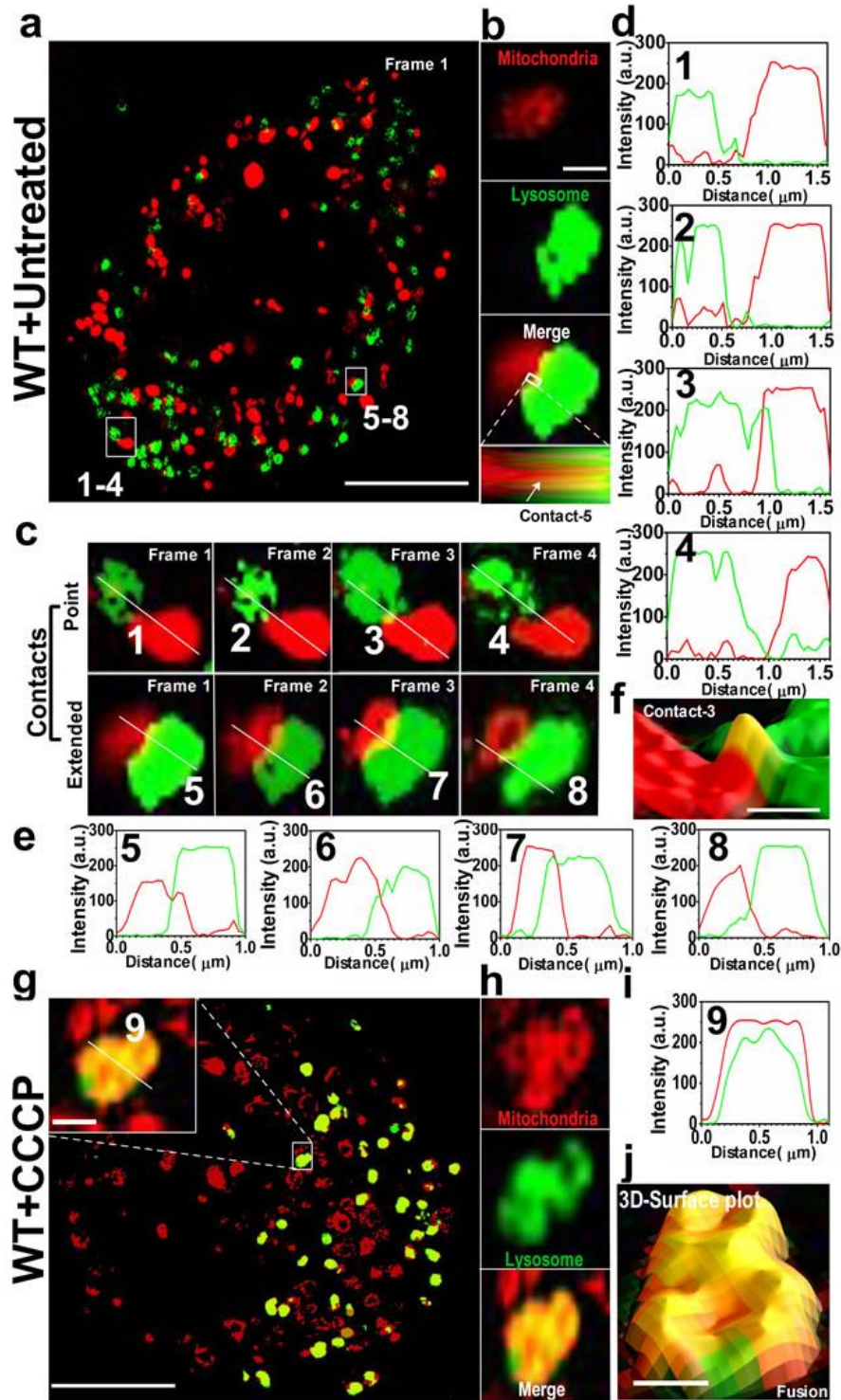
514 intensity in the dynamic process of approach. **(c)** Trend of fluorescence intensity in the dynamic process

515 of separation. **(d-f)** Frames 1-3 of the dynamic approach process in the red rectangle of **(a)**. **(g-i)** Frames

516 4-6 of the dynamic separation process in the blue rectangle of **(a)**. The time interval between each frame

517 is approximately 2 s. Both red and blue solid lines show fluorescence intensity. Scale bars: **(a)** 5 μm, **(d)**

518 1 μm.



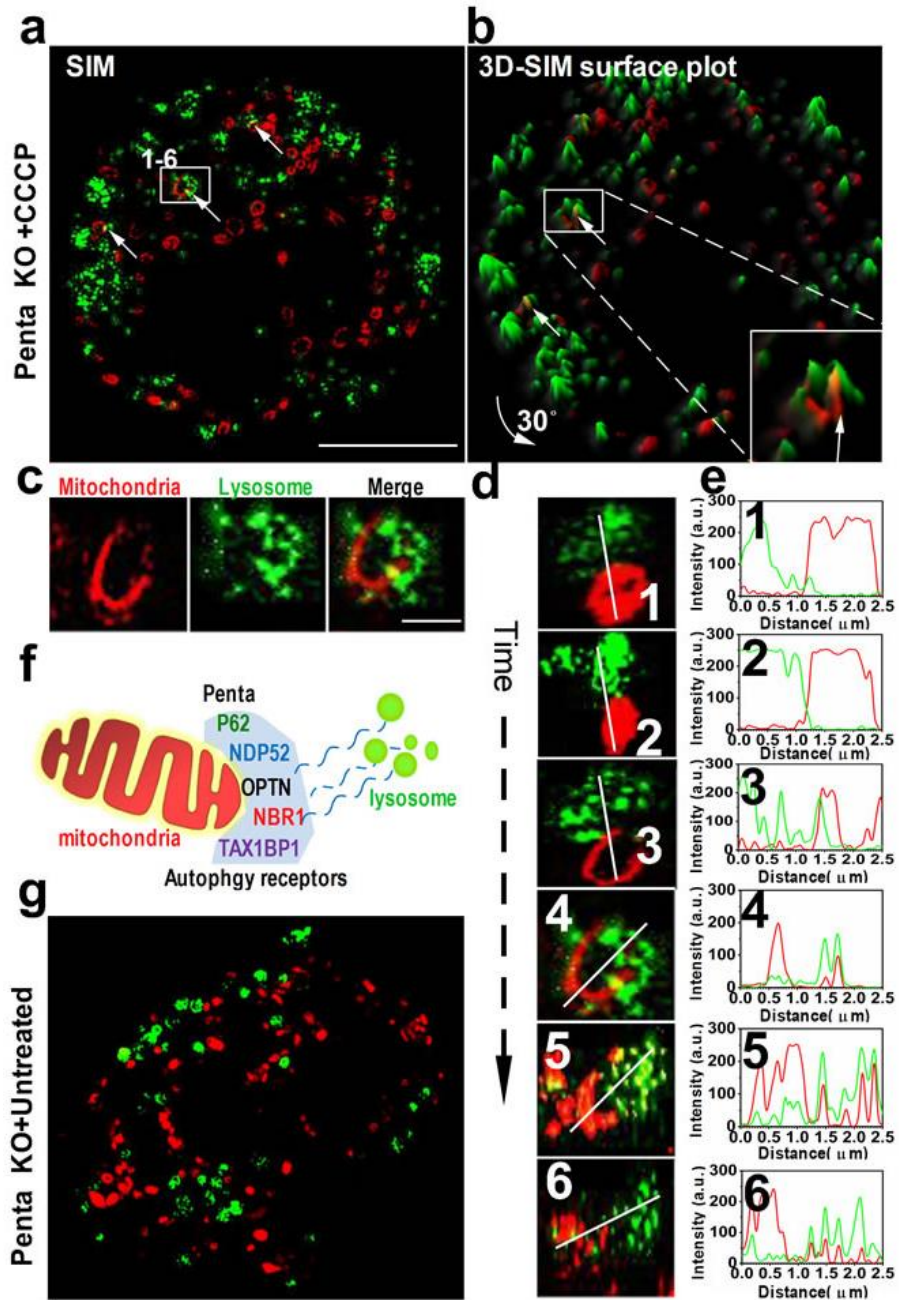
519

520 **Figure 4 Iridium(III) complex dye tracking of mitochondria-lysosome contact (MLC) and fusion**

521 **events in living cells. (a) MLC events in WT cells. White rectangles represent two types of MLCs, point**

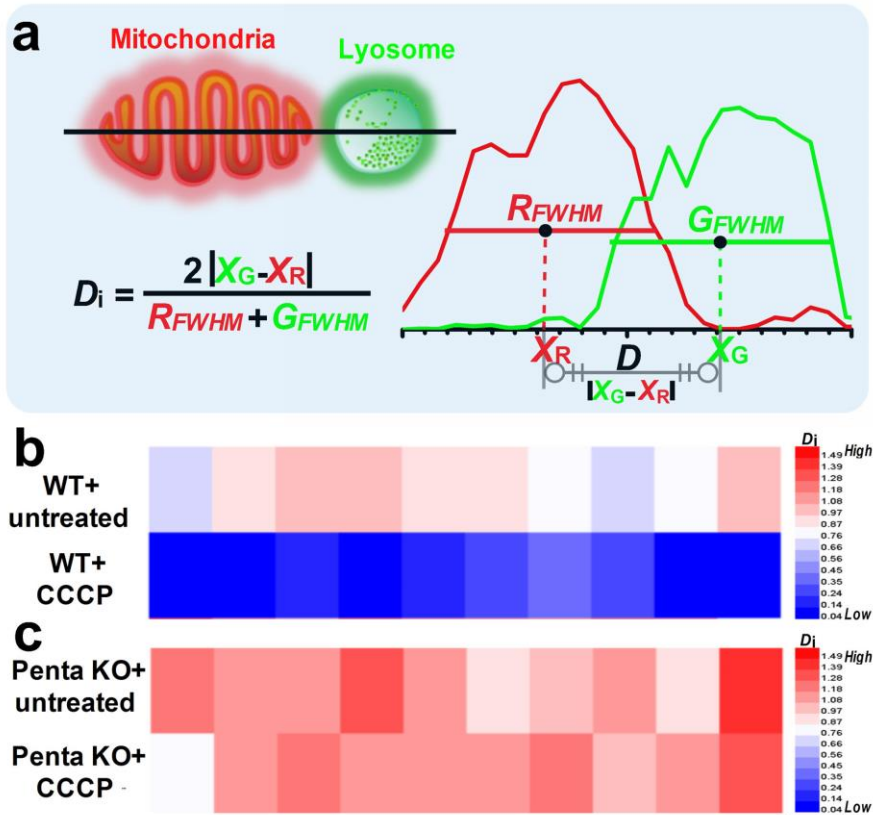
522 **(1-4) and extended (5-8) contacts. (b) A representative MLC event. White rectangle represents the**

523 amplification. **(c)** Point and extended MLCs in **(a)**. White solid lines indicate the fluorescence intensity
524 shown in **(d)** and **(e)**. **(f)** Partial enlargement of **(d)**-3. **(g)** Fusion events in WT cells after treatment
525 CCCP. White rectangle shows the representative fusion event, and the white solid line shows
526 fluorescence intensity. **(h)** A representative fusion event detected by using the iridium(III) complex dye
527 (red, mitochondria) and LysoTracker Green (green, lysosome). **(i)** Fluorescence intensity of the solid
528 line of **(g)**-9 inset. **(j)** 3D SIM surface plot of merged image in **(h)**. Scale bars: **(a)** 5.0 μm , **(b)** 0.5 μm , **(e)**
529 0.2 μm , **(g)** 5.0 μm , **(g)**-9 0.5 μm , **(j)** 0.5 μm .



530

531 **Figure 5 Iridium(III) complex dye for tracking MLC in Penta knockout HeLa cells. (a)** MLC
532 events in Penta KO cells treated with 10 μM CCCP for 12 h. White rectangle represents the MLC shown
533 in (d). (b) 3D SIM surface plot of (a) after 30-degree rotation. White arrows indicate the MLC events. (c)
534 A representative MLC event. (d) Time evolution of one MLC in living cell. White solid lines indicate
535 fluorescence intensity shown in (e). Scale bars: (a) 5.0 μm, (b) 1.0 μm.



536

537 **Figure 6 Quantitative analysis of the interaction between mitochondria and lysosomes.** (a) The
 538 schematic illustration of a D_i value for quantitative analysis of the distance between mitochondria and
 539 lysosomes. R_{FWHM} indicates the FWHM of red color (mitochondria); G_{FWHM} indicates the FWHM of
 540 green color (lysosomes); X_R indicates the X-axis value of the R_{FWHM} center; and X_G indicates the X-axis
 541 value of the G_{FWHM} center. (b) D_i values of mitochondria and lysosome in WT cells with or without
 542 CCCP treatment (n = 10). (c) D_i values of mitochondria and lysosome in Penta KO cells with or without
 543 CCCP treatment (n = 10).